processes

MDPI

Article

Influence of Cyclic Loading Parameters on Sand-Production Characteristics and Particle-Size Distribution in Gas Storage

Wenhong Zhang [1], Hantao Zhao [1], Tianyu Wang [1], Junjie Xue [2], Yawen Tan [3] and Shouceng Tian [3,*]

[1] State Key Laboratory of Petroleum Resources and Engineering, China University of Petroleum-Beijing, Beijing 102249, China; 2021310153@student.cup.edu.cn (W.Z.)
[2] Oil and Gas Technology Institute of Changqing Oilfield Company, PetroChina, Xi'an 710018, China
[3] Karamay Branch of State Key Laboratory of Petroleum Resources and Engineering, China University of Petroleum-Beijing at Karamay, Karamay 834000, China
* Correspondence: tscsydx@163.com

Abstract

Depleted oil and gas reservoirs, owing to their large storage capacity and well-established infrastructure, are attractive sites for storing green energy carriers such as natural gas, hydrogen, and compressed air. During injection–production cycling in underground gas storage (UGS), variations in effective stress can cause repeated stress disturbances in the reservoir and surrounding rock, which may trigger borehole sand production. In this study, laboratory sand-production simulation tests were conducted to evaluate the effects of cyclic-loading stage, upper stress limit, and cycling frequency on borehole damage and sand-production behavior. The results show that sand production is stage-dependent. During the rapid-hardening and stable stages, the borehole remains largely intact and sand production is negligible. Once the failure and collapse stages are reached, borehole integrity deteriorates and sand production increases sharply, with fine particles becoming dominant. Cumulative sand production increases with the upper stress limit. Increasing the upper limit from 80% to 95% leads to a 2.53-fold increase in produced sand mass, together with a higher fine-sand fraction and a shift in the particle-size distribution (PSD) toward smaller sizes. The cycling frequency also plays an important role. When the frequency decreases, cumulative sand production increases and becomes 53.1% higher than the baseline at 0.001 Hz. Meanwhile, the median particle size (D50) decreases, indicating stronger particle breakage under low-frequency cycling. These findings provide guidance for designing injection–production schemes for UGS and for selecting appropriate sand-control completion strategies.

Keywords: underground gas storage; cyclic loading; sand production; particle size distribution; cyclic loading parameters

Check for updates

Academic Editor: Qingbang Meng

Received: 27 December 2025
Revised: 21 January 2026
Accepted: 26 January 2026
Published: 28 January 2026

Copyright: © 2026 by the authors. Licensee MDPI, Basel, Switzerland. This article is an open access article distributed under the terms and conditions of the Creative Commons Attribution (CC BY) license.

1. Introduction

Under China's dual-carbon goals and the ongoing energy transition, large-scale energy storage in subsurface space has become a key approach to enhance energy-system flexibility and security [1–3]. Depleted oil and gas reservoirs are widely regarded as suitable geological media for natural gas storage. This is mainly due to their large effective storage capacity and good sealing integrity, as well as existing well patterns and surface pipeline infrastructure. Depleted oil and gas reservoirs also provide potential for storing other green energy carriers, such as hydrogen and compressed air. Unlike conventional reservoirs operated under continuous and quasi-steady production, gas-reservoir-type underground

gas storage (UGS) typically follows a seasonal injection–withdrawal schedule characterized by high-rate injection and high-rate production. Gas is injected during the low-demand period in summer and withdrawn during the peak-demand period in winter to mitigate peak-shaving pressure associated with regional supply–demand imbalance. Such alternating injection–production operations induce persistent pore-pressure fluctuations, thereby causing repeated variations in formation effective stress and near-wellbore stress paths [4]. These repeated stress perturbations facilitate cyclic damage accumulation, pore-structure evolution, and progressive strength degradation in both the reservoir and the surrounding rock. Consequently, the near-wellbore zone becomes more susceptible to sand production, accompanied by engineering hazards such as plugging and erosion [5–7]. Compared with conventional oil and gas reservoirs, UGS systems undergo multiple injection–production cycles throughout their service life. This results in stronger and more frequent stress disturbances, leading to higher sanding risk, more severe sand production, and more complex underlying mechanisms. Therefore, investigating the failure evolution of reservoir rock and the associated sand-production responses under cyclic (alternating) loading is of both theoretical and engineering significance. Such understanding supports efficient UGS development, safe high-rate operation, optimization of injection–production schemes, and the design of sand-control completions.

With the large-scale construction and commissioning of underground gas storage (UGS) facilities, sand production has been increasingly reported in UGS sites both in China and worldwide. It has become a prominent engineering problem that compromises operational safety and efficiency. For example, sanding occurred during the operation of the Wen 96 UGS in China. As a result, 2–3 choke beans (choke nozzles) had to be replaced within a single gas-withdrawal cycle, and erosion failure of the control-valve trim (valve plug) was observed in 12 wells [8]. After sand production occurred in the Hutubi underground gas storage (UGS) in Xinjiang, the daily gas production rate declined from 8.0×10^5 m^3 to 4.0×10^5 m^3, indicating substantial deliverability loss [9]. Similar risks have also been reported in overseas underground gas storage (UGS) facilities. For example, a large amount of sand was produced near the end of the withdrawal period in the Redfield & Vincent UGS (USA), which triggered three wellsite fires. Sand erosion further caused tubing perforation, markedly increasing operational safety hazards [10]. In the Hungarian underground gas storage (UGS) facility developed from the Hajdúszoboszló gas reservoir, the reservoir sanding risk exceeds 70%, posing a potential threat to long-term stable operation. Overall, sand production in underground gas storage (UGS) is widespread and highly detrimental. Systematic studies on its controlling factors are urgently needed to support optimization of injection–production schemes and the development of sand-control strategies. To address this issue, previous studies have examined cyclic load-induced damage and sanding-risk assessment. It is generally accepted that, under "strong injection–strong production" alternating operation in gas-reservoir-type UGS, periodic fluctuations in pore pressure and effective stress can markedly modify the near-wellbore stress path and induce cyclic damage. Consequently, UGS reservoirs exhibit a higher sand-production risk and more complex mechanisms than conventional oil and gas reservoirs [11]. Kang evaluated carbonate-reservoir core samples from the Xiangguosi underground gas storage (UGS) by conducting stress-sensitivity and velocity-sensitivity tests, together with core-flow (core-flooding) experiments under UGS operating conditions. The results showed that pressure fluctuations are a key trigger for migration of fine sand in UGS reservoirs [12]. Dong noted that long-period, high-rate alternating injection–production in UGS causes cyclic variations in stress, flow direction, and the gas–water interface. This makes sand-production prediction and mitigation more challenging [13]. Sui performed alternating-load sanding tests and modified a sanding index by incorporating the damage level, number of loading cycles,

and loading frequency. This enabled sanding-risk assessment and sanding-onset time prediction, providing support for sand-control completion and production-scheme design [14]. Ma et al. conducted high-pressure sanding experiments and identified two critical thresholds, namely, an equivalent initial sanding pressure and the collapse pressure, which can be predicted by a thick-walled cylinder model. Staged changes in sand production as well as particle size were reported when the confining pressure exceeded the corresponding thresholds, providing an experimental basis for quantifying hole-failure-controlled sanding [15]. McLellan et al. systematically examined sand production from the perspectives of completion design and risk assessment, with particular attention to hole/perforation collapse, reservoir-pressure variation, and cyclic-loading-induced strength reduction. In addition, the adverse impact of overly conservative sand-control designs on injection–production capacity was highlighted [16]. Zhang et al. employed China's first sand-production simulation apparatus for underground gas storage (UGS) to conduct alternating-load sanding tests on an offshore UGS developed in unconsolidated sandstone. The experiments indicated that alternating loading, together with flow rate, constitutes a key factor governing sanding in unconsolidated sandstone reservoirs [17]. Hou and Liao evaluated operating conditions, including formation pressure, water content (water cut), and flow rate/pressure drawdown. The analysis indicated that low formation pressure and elevated water content aggravate sand production, whereas critical ranges and plugging effects occur with respect to flow rate and effective stress. Owing to limitations of the experimental setups, the influence of cyclic alternating operating schemes in UGS was not incorporated [18,19]. Song et al. performed laboratory mechanical tests to assess the effects of water-content variation and cyclic loading on sandstone properties. Pronounced strength degradation was observed with increasing water content and an increasing number of cycles. Based on these observations, damage evolution associated with water content and cyclic loading was parameterized, providing key mechanical inputs for calculating and predicting the critical drawdown pressure (CDP) for sanding [20]. Tian et al. investigated alternating loading through fatigue-damage experiments combined with discrete element method (DEM) simulations. The results suggested that appreciable damage emerges only after the rock enters the plastic regime. The effects of stress upper/lower limits and loading rate were further ranked, while a hole-scale effect was identified, offering insights for predicting the critical pressure drawdown for sanding under alternating loading [21]. Collectively, prior work indicates that sanding mechanisms under UGS operating conditions differ from those under conventional production. Nevertheless, mechanistic understanding remains incomplete. Existing studies predominantly emphasize final sand yield or CDP, whereas systematic investigation of hole-failure morphology evolution across different stages of cyclic loading, together with the periods of abrupt sanding escalation, remains limited. Fine sand represents a major operational risk because fine sand readily plugs screens and accelerates tubular erosion; however, the current understanding of the proportion of fine sand and its particle-size refinement, as well as its relationship with geometric features of hole damage, is still insufficient. Moreover, the influence of cycling frequency has often been addressed via empirical corrections or statistical correlations, leaving the role of frequency in governing grain crushing and particle-size distribution evolution under cyclic loading insufficiently explored. Previous studies have indicated that spatial variability in grain-size distributions, together with permeability heterogeneity, can significantly influence fine-sand generation and particle mobilization in sand-prone formations. Grain-size variability inferred from gamma ray measurements and permeability-based assessments has been used to capture spatial differences in particle-size distributions and fine-sand susceptibility in outcrops [22,23]. These observations highlight the importance of considering inherent grain-scale heterogeneity when interpreting sand-production behavior, particularly under

cyclic stress conditions. To address these gaps, the present study conducted sanding experiments under UGS-type cyclic loading using outcrop red sandstone collected from the Xinjiang M UGS area. The effects of loading stage, stress amplitude, and cycling frequency on sanding behavior were investigated. Multi-scale characterization—including sieving, laser particle-size analysis, and quantitative CT-image analysis—was further applied to elucidate the associated sanding mechanisms, thereby providing more direct support for optimizing UGS injection–production schemes and designing sand-control completions.

2. Sand-Production Experiments Under Cyclic Loading for Underground Gas Storage

2.1. Core Sample Preparation

The experiments employed red sandstone samples from the reservoir of the M underground gas storage (UGS). The porosity ranged from 21.6% to 22.8%, and the permeability ranged from 210.8 to 305.6 mD, indicating a medium-porosity and medium-permeability sandstone. Whole-rock mineralogical composition was determined by X-ray diffraction (XRD) using a Bruker D8 Focus diffractometer (Bruker Corporation, Bruker AXS SE, Karlsruhe, Germany). Mineralogical analysis indicated that the sandstone contained 57% quartz, 5.2% K-feldspar, 20.9% plagioclase, 6.2% calcite, 2.1% ankerite (ferroan dolomite), and 8.6% clay minerals, with quartz and feldspar as the dominant constituents. As shown in Figure 1, petrographic thin-section photomicrographs indicate that intergranular pores are the primary pore type in the M UGS reservoir. Quartz commonly exhibits secondary overgrowth, while feldspar generally shows dissolution features.

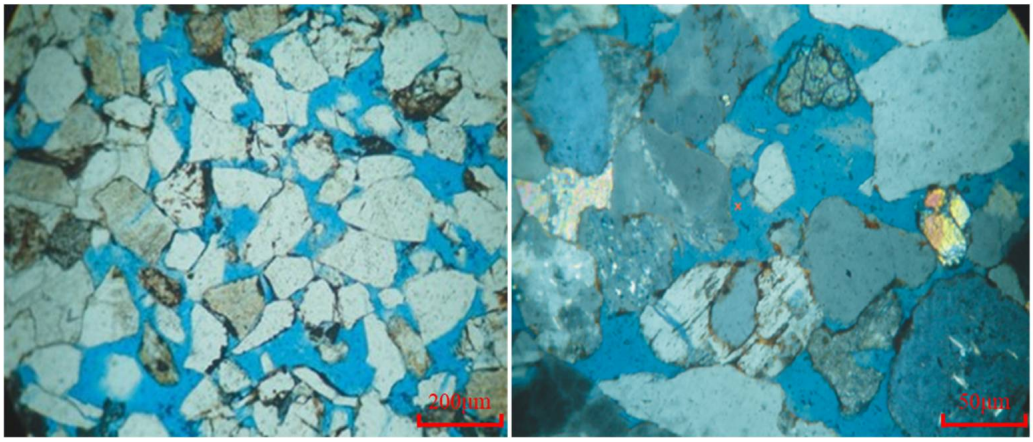


Figure 1. Petrographic thin-section photomicrograph.

As shown in Figure 1, the rock blocks were machined into standard cylindrical specimens using a TX-SHM200C programmable double-end surface grinder (Taizhou Xinyu Instrument Equipment Factory, Taizhou, China). The specimens were 50 mm in diameter and 100 mm in length, and the machining tolerance met the requirements of international rock mechanics testing standards. To minimize the influence of specimen heterogeneity on the experimental results, the P-wave (longitudinal wave) velocity was measured with an RSMSY5 ultrasonic tester (Wuhan Zhongyan Technology Co., Ltd., Wuhan, China). Only specimens with no visible defects and a P-wave velocity variation within 5% were selected for subsequent experiments [24].

The thick-walled cylinder sand-production test was designed to replicate downhole perforation-tunnel conditions. Therefore, a mechanical hole was drilled at the center of each core sample to create an artificial perforation. Dry drilling on a lathe was adopted to keep the hole centered and to avoid hydration effects on the rock properties. After drilling, residual chips were removed using compressed air. Based on the geometric similarity

criterion with an outer-diameter-to-hole-diameter ratio of 3:1, the hole diameter was set to 16 mm and the drilling depth was 60 mm, leaving a 40 mm intact section at the bottom [25]. Figure 2 shows the core samples and the drilling geometry.

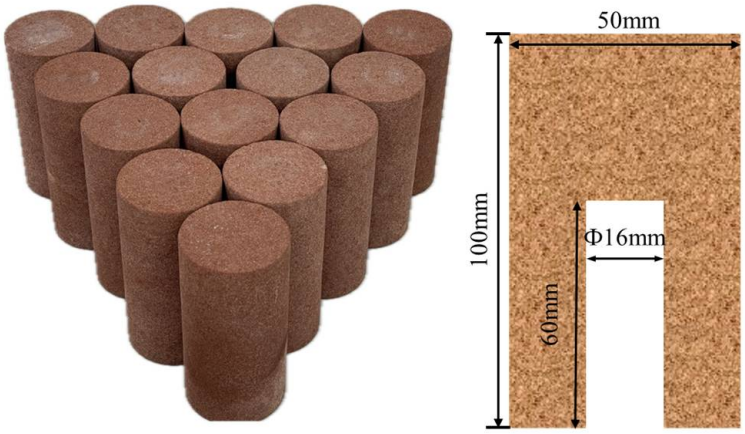


Figure 2. Core samples and drilling geometry.

2.2. Experimental Set-Up

A laboratory-scale thick-walled cylinder sand-production experiment was designed to investigate the controlling factors of sand production in underground gas storage (UGS) under cyclic loading. As shown in Figure 3, the experiments were conducted using a GCTS-RTR-1000 rock mechanics testing system. To enable direct observation of hole damage during loading, a visualized sand-production apparatus was developed. A miniature camera with an integrated light source, together with a signal acquisition system, was installed on the loading head of the core sample. As shown in Figure 4, the morphological evolution of the hole could be continuously recorded after the test had started. Based on the real-time camera observations, the confining pressure was increased until the core sample fractured and sand production occurred. This pressure (75 MPa) was defined as the critical confining pressure for sand production. Subsequent cyclic-loading sand-production tests were then performed by applying cyclic loading at prescribed ratios relative to the critical confining pressure to examine sand-production behavior under different cyclic parameters.

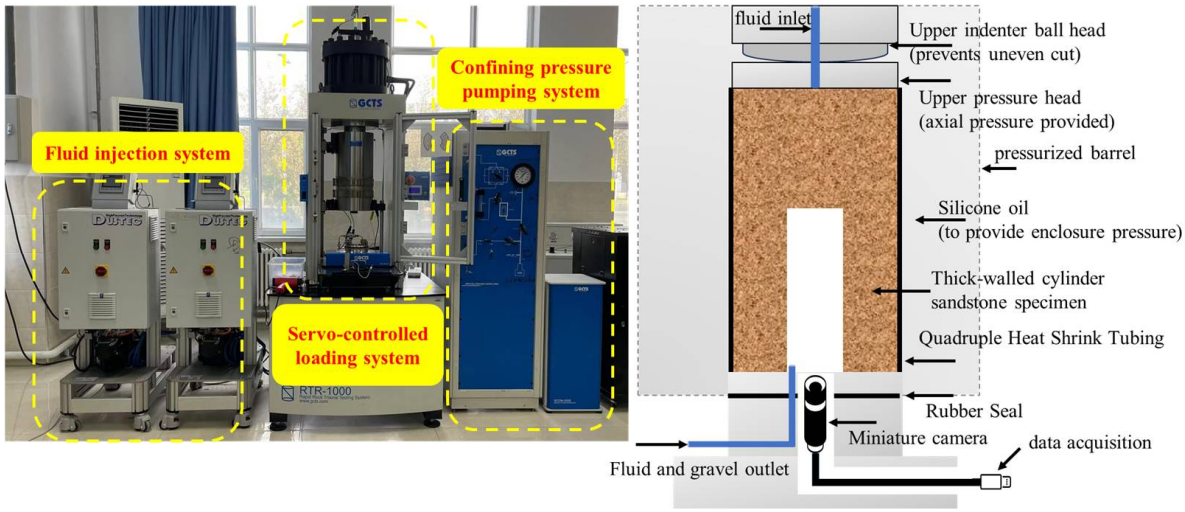


Figure 3. Laboratory apparatus for UGS sand-production experiment.



Figure 4. Sand-production morphology around the borehole during cyclic loading.

2.3. Experimental Scheme

First, two monotonic confining-pressure ramp tests were performed under an axial stress of 2 MPa. Confining pressure was continuously increased until sand production occurred at the borehole; the corresponding confining pressure, approximately 75 MPa, was defined as the reference value for subsequent tests. Subsequently, under the same axial stress, one set of confining-pressure cyclic loading–unloading tests was conducted to simulate the cyclic loading process in underground gas storage, and the test was continued until fatigue failure of the rock occurred. As shown in Figure 5, after collapse induced by cyclic loading, the radial strain remained in a compressive state (positive values), and the confining pressure–radial strain curve exhibited a distinct stress hysteresis loop. The confining pressure–radial strain response can be divided into four stages: rapid hardening, stable, failure, and collapse. The four stages were coded as 1, 2, 3, and 4, respectively. The tests were terminated when the cyclic response entered the specified stage interval, so as to compare differences in sand-production behavior under different injection–production cycle durations. For the cyclic upper limit, four stress levels (95%, 90%, 85%, and 80%) were adopted to simulate conditions below the critical sand-production pressure and to evaluate the effect of different cyclic upper-pressure limits on sand production in UGS. Considering the influence of injection–production frequency during UGS operation, while keeping the loading path unchanged, the cyclic loading frequencies were set to 0.033 Hz, 0.017 Hz, 0.0033 Hz, and 0.001 Hz. Because the actual injection–production frequency in field operations cannot be fully replicated in the laboratory, these frequencies were varied to investigate the time-dependent effect of injection–production cycling on sand production.

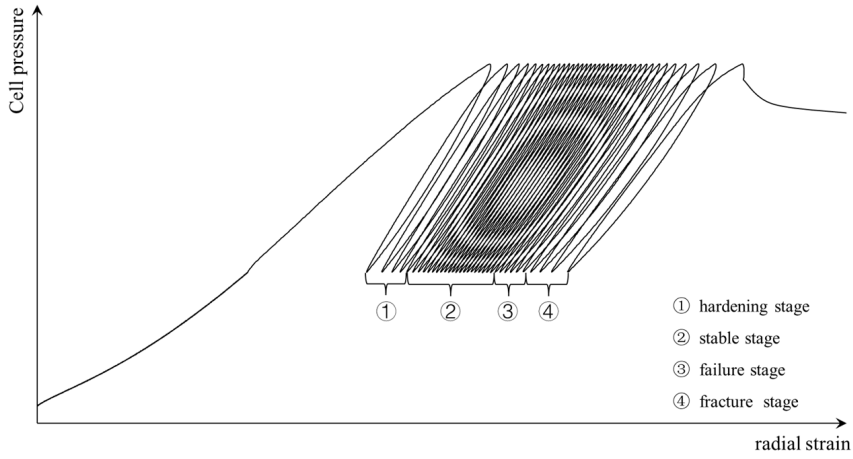


Figure 5. Schematic of the cyclic confining pressure–radial strain relationship.

The loading waveform is shown in Figure 6. A triangular stress waveform was adopted to represent the cyclic pressure variations associated with injection–production operations in underground gas storage. Field operation data indicate that the injection–production pressure typically varies from 18 to 38 MPa, corresponding to a fluctuation range (amplitude) of 20 MPa [26,27]. Accordingly, the cyclic stress amplitude in the laboratory tests was set to 20 MPa, consistent with the pressure fluctuation range observed under actual operating conditions. The reference value for the upper confining-pressure limit was taken as the critical sand-production pressure. In total, 10 test groups were designed to investigate the effects of injection–production cycle duration, the cyclic upper stress level, and cyclic loading frequency on sand production in UGS. The experimental matrix is summarized in Table 1.

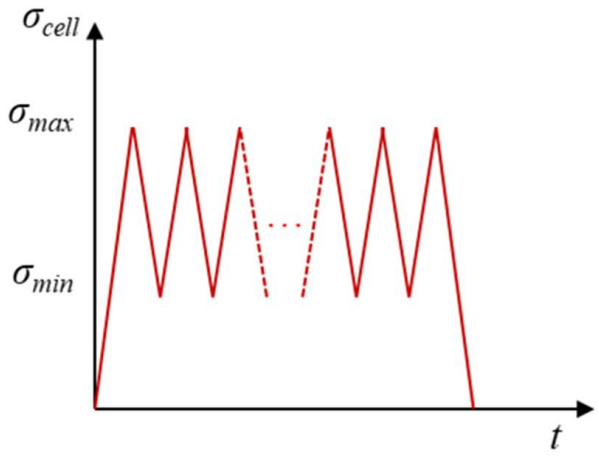


Figure 6. Schematic diagram of the cyclic loading waveform.

Table 1. Experimental program.

Core ID	Upper Stress Level	Unloading Stage (No.)	Cycling Frequency (Hz)
1#–4#	0.9	1/2/3/4	0.033
5#–7#	0.8/0.85/0.95	4	0.033
8#–10#	0.9	4	0.017/0.0033/0.001

2.4. Experimental Procedure

The main experimental procedures were as follows: (1) The thick-walled cylinder core was placed on a 50 mm-diameter base. The upper platen, core, and lower platen were wrapped with a double layer of heat-shrink tubing and heated until fully shrunk and sealed, in order to prevent external silicone oil from entering the core's interior. (2) The upper loading head of the GCTS RTR-1000 system was slowly lowered onto the top surface of the core, and an axial stress of 2 MPa was applied. The confining-pressure cell was then lowered to the bottom sealing ring, and silicone oil was injected into the cell to provide the required confining pressure. (3) Nitrogen was injected through the top inlet using a Dustec dual-piston displacement pump to establish a steady flow. Based on field data (effective reservoir thickness of 31.8 m, daily gas injection rate of 21 $\times$ 10^4 m^3/d per well, and a 7-inch wellbore diameter), the laboratory injection rate was determined following the calculation method proposed by Liao Wei [18], and 2 L/min was selected as the gas injection rate. (4) Confining-pressure cyclic loading tests were carried out according to the experimental design. After each test, the loose sand that had accumulated in the hole was collected, weighed using an electronic balance, and recorded as the produced sand mass. (5) After the tests, the particle-size distribution of the produced sand was measured using a Malvern laser particle size analyzer with a measurement range of 0.02–2000 μm. In addition, CT

scanning was performed to reconstruct the hole's inner wall and to characterize the hole damage and failure features.

3. Results and Discussion

3.1. Effects of Cyclic-Loading Stages on Sand Production

Figure 7 shows the sand-production process and the evolution of cumulative produced sand mass for core samples with different IDs at various stages under cyclic loading. For Cores #1 and #2, the hole geometry remained stable during the rapid-hardening and stable stages, and no noticeable damage or sand production was observed. For Core #3, the hole remained relatively intact in the early stages. In the failure stage, slab-like spalling appeared on the hole wall. Localized damage then propagated in the axial direction. Sand production started at this stage. Core #4 experienced a full progression from rapid hardening and stability to failure and ultimate collapse. With continued cycling, hole integrity progressively deteriorated, and symmetric compressive-failure zones formed along the hole axis. In the collapse stage, sand production from the failed zones intensified, and the damage evolution shifted from predominantly axial propagation to extension into the surrounding rock, with abundant fine loose particles detaching and accumulating in the hole. The cumulative sand-mass histogram indicates a sharp increase in sand production after entering the failure stage, whereas negligible amounts of sand production occurred during the early cycling period.

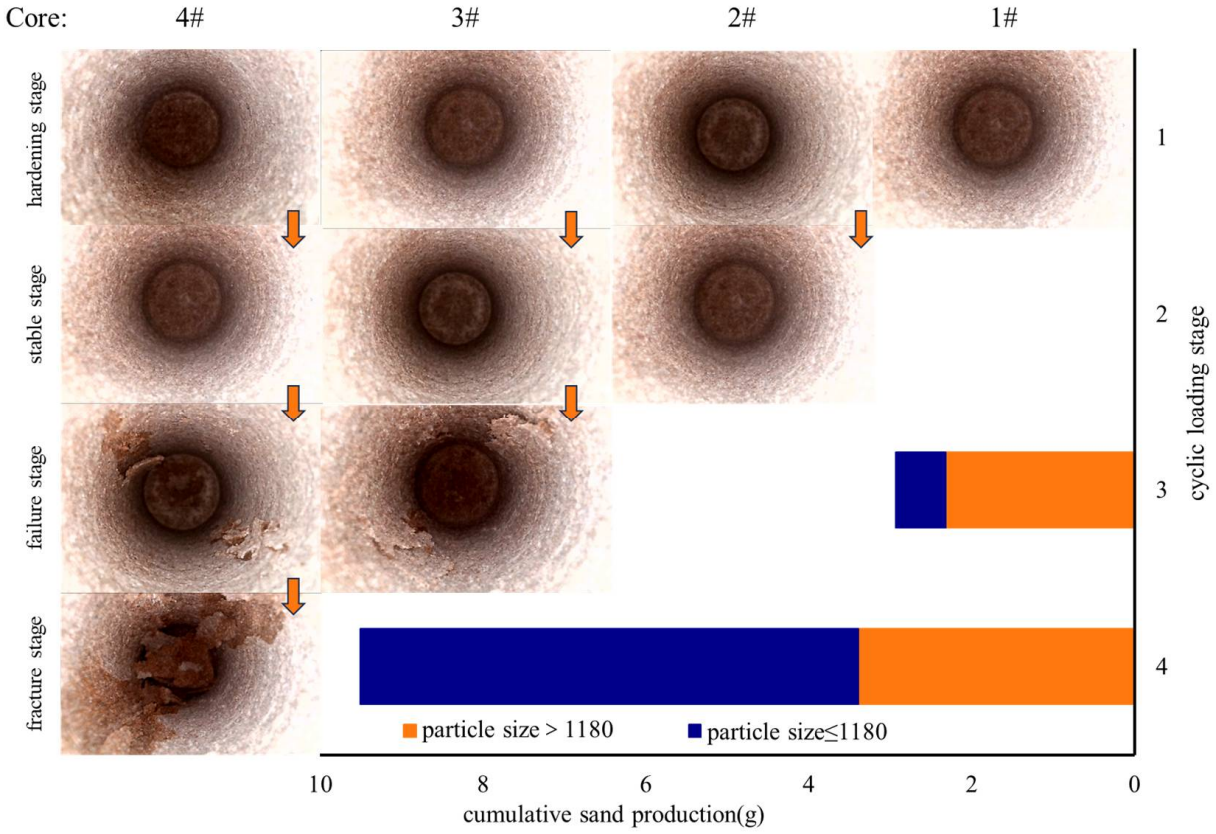


Figure 7. Hole morphology and cumulative sand production at different cyclic loading stages.

After the sand-production tests, the produced sand and the residual material remaining in the hole were collected. A sieve analysis was performed to characterize the produced sand, and particles were classified into coarse and fine fractions using a 1180 μm sieve [28]. Figure 8 shows that the particle-size distribution of the produced sand and the cumulative produced-sand mass varied markedly across the cyclic-loading stages. As the specimens

evolved from the rapid-hardening stage to the collapse stage, the cumulative produced sand mass increased continuously, and the mass contributions of both coarse and fine fractions increased to different extents. In the early stage of sand production, the produced sand was dominated by coarse agglomerates, accounting for 79.17% of the total produced sand mass. After the specimens entered the collapse stage, the produced sand mass rapidly increased to 9.25 g, which is 3.24 times that in the failure stage, while the proportion of coarse sand decreased significantly. Combined with the visual observations, these results confirm that fine particles became the primary source of produced sand in the later stage. Comparisons between the two test stages indicate that the mass of coarse produced sand changed only slightly, whereas the overall variation in sand production was mainly governed by the fine-sand fraction.

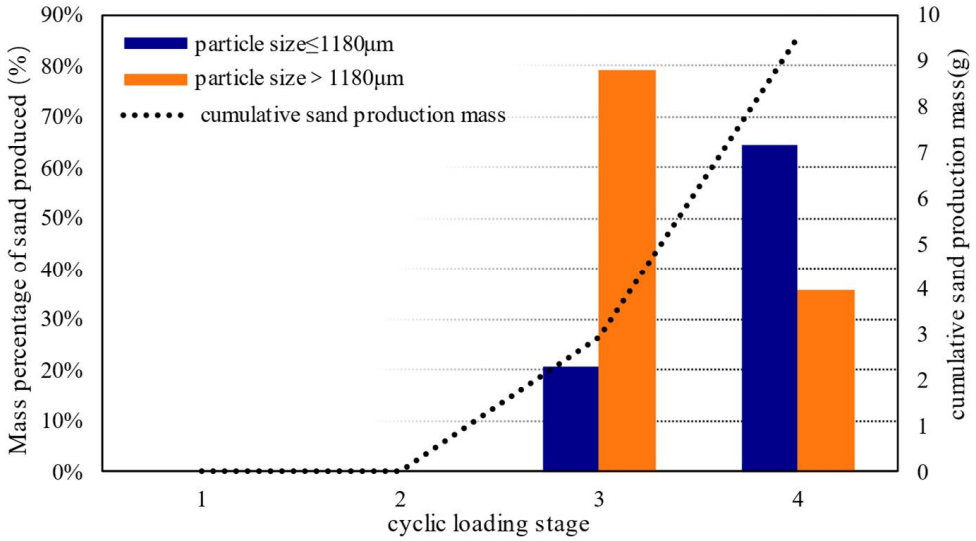


Figure 8. The proportion of different particle-size fractions at different cyclic loading stages.

In sieve analysis for formation-sand particle-size characterization, the largest sieve opening commonly used is 1180 μm. Particles larger than 1180 μm are typically not further subdivided into finer size classes. Therefore, in this study, 1180 μm was adopted as the threshold to distinguish fine and coarse fractions in the produced sand [28]. In contrast, fine sand poses a higher risk of equipment plugging and erosional wear due to particle impingement, leading to more severe impacts on production performance and sand-control design. Accordingly, the production characteristics of fine sand during cyclic loading warrant particular attention. In the experiments, the separated fine-sand fraction was analyzed for particle-size distribution using a Malvern laser particle-size analyzer. As shown in Figure 9, the median particle size (D50) was 48.4 μm for Group #3 and 50.0 μm for Group #4. From the differential (frequency) distribution curves, the peak particle size of Group #4 is smaller than that of Group #3. From the cumulative volume distribution curves, the cumulative curve of Group #3 lies overall below that of Group #4, indicating a lower cumulative volume fraction for Group #3 at the same particle size. Moreover, Group #4 reaches 100% cumulative volume fraction more rapidly, suggesting that the cumulative contribution of smaller particles increases faster in Group #4 and that relatively finer particles account for a higher proportion of the produced sand. In addition, the cumulative curve of Group #3 reaches 100% only after extending into the coarser size range, implying that the produced sand from Group #3 contains a higher proportion of coarse particles compared with Group #4.

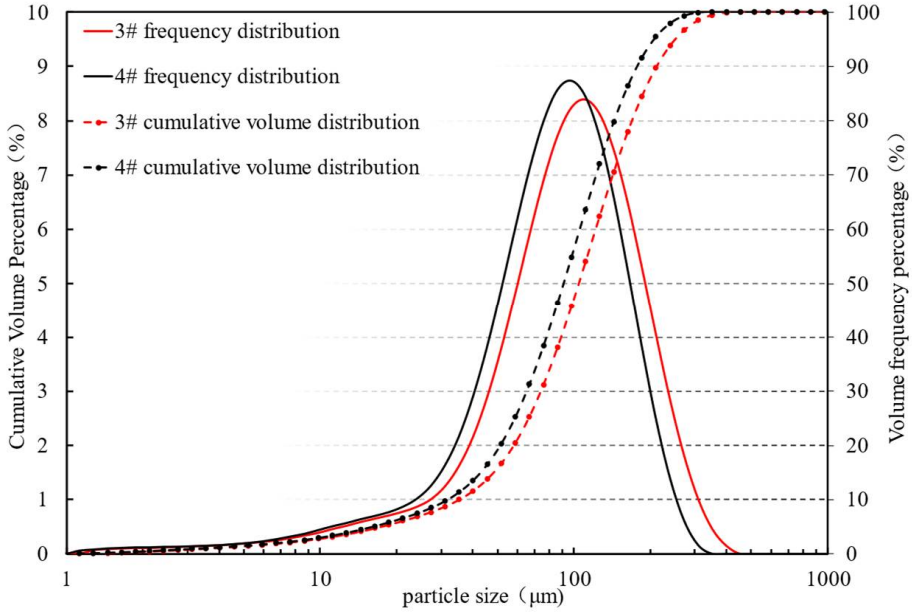


Figure 9. Particle-size distribution of the produced fine sand.

To investigate the influence of different cyclic-loading stages on hole fragmentation during sand production, CT scanning was performed on the core samples after the tests to capture the internal and external damage around the hole; the results are shown in Figure 10. Figure 10 illustrates the hole characteristics of the specimens after being subjected to different stages of cyclic loading. The newly formed fractured area was quantified using ImageJ (Version 1.54p, https://wsr.imagej.net/notes.html, accessed on 17 February 2025). Upon entering the failure stage, the newly fractured area reached 92.09 mm^2. At this stage, a V-shaped dog-ear failure pattern developed, with symmetric fractured zones formed along the axial direction; the damage was mainly concentrated in the middle-to-lower part of the hole depth, and the damaged area of the hole began to increase. In the collapse stage, the newly fractured area further increased to 173.60 mm^2. Extensive spalling occurred with substantial sand production, and the hole exhibited large areas of damage with pronounced axial extension; the fractured area expanded from the middle-to-lower section in the failure stage to nearly the top and bottom ends. In terms of the increase factor, the newly fractured area in the collapse stage was approximately 1.89 times that in the failure stage. Overall, as cyclic loading progressed from the rapid-hardening and stable stages to the failure and collapse stages, hole damage continuously intensified. Correspondingly, sand production evolved from negligible to limited and then to substantial, while the hole morphology transitioned from relatively intact to extensive damage accompanied by axial propagation.

3.2. Effects of the Stress Upper Limit Under Cyclic Loading on Sand Production

The upper stress limit is an important parameter in cyclic loading. To clarify the sand-production behavior at different upper limits, sand-production tests were carried out in the collapse stage, where sand production was the most evident. The upper limits were set to 80%, 85%, 90%, and 95%. Figure 11 shows the cumulative produced sand mass under these conditions. The cumulative sand mass increased clearly as the upper limit rose from 80% to 95%. At an upper limit of 95%, the cumulative sand mass increased sharply and was about 2.53 times that at 80%. In addition, as shown in Figure 12, the produced sand was still dominated by fine particles. With a higher upper limit, the fraction of fine sand increased, while the fraction of coarse sand decreased. The fine-sand fraction was ~59.20% at 80% and increased to 70.52% at 95%. These results indicate that a higher upper

stress limit not only increases the amount of produced sand but also shifts the particle-size distribution toward finer particles.

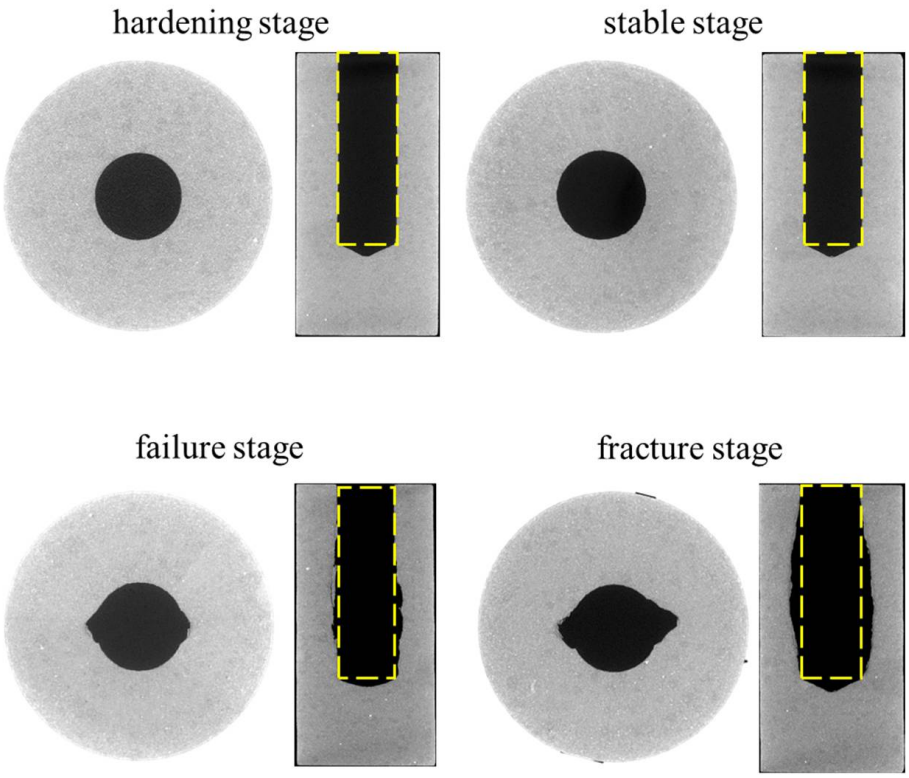


Figure 10. Borehole damage at different stages of cyclic loading.

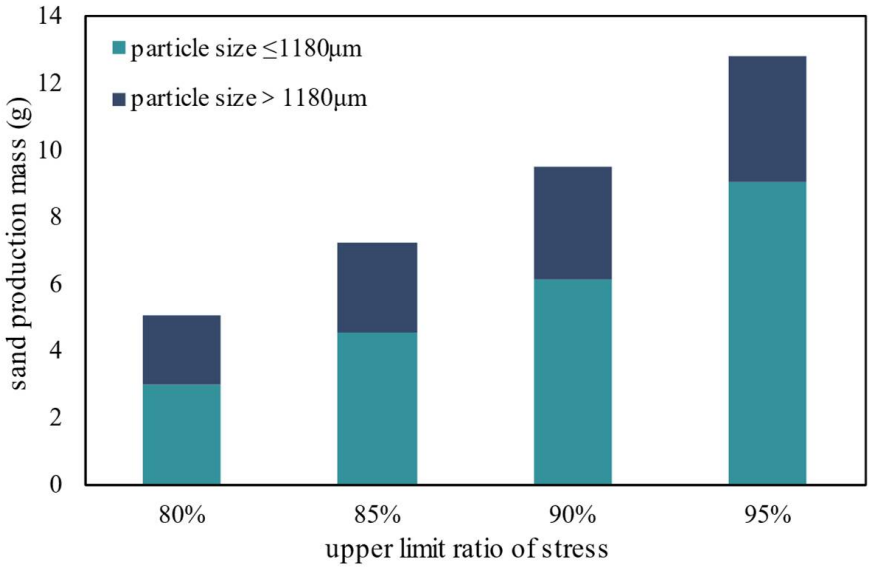


Figure 11. Cumulative sand production at different upper cyclic stress limits.

The fine-sand fractions produced under different cyclic upper stress limits were analyzed by laser diffraction particle-size measurement. Figures 13 and 14 present the particle-size frequency distributions and cumulative volume distributions, respectively. In the frequency distributions, the curves shift toward smaller particle sizes as the cyclic upper stress limit increases, indicating progressive particle-size refinement. At upper stress limits of 90% and 95%, the modal size range remains unchanged, whereas the peak magnitude differs; relative to the 90% group, the 95% group exhibits higher volume fractions over

most of the finer-size domain. Overall, the produced sand becomes finer with increasing cyclic upper stress limits. In the cumulative volume distributions, a higher upper stress limit leads to a steeper rise in cumulative volume percentage. Consistently, the median particle size (D50) decreases from 127.6 μm at 80% to 113.6 μm at 85%, 92.4 μm at 90%, and approximately 87.8 μm at 95%, confirming a monotonic reduction in D50 with increasing cyclic upper stress limit.

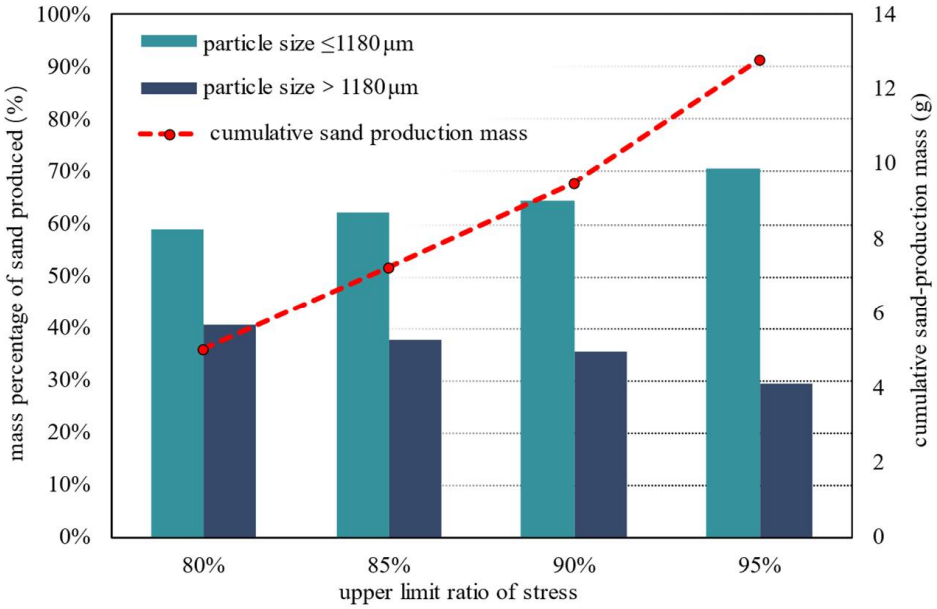


Figure 12. Mass fractions of produced sand in different particle-size ranges under different cyclic upper stress limits.

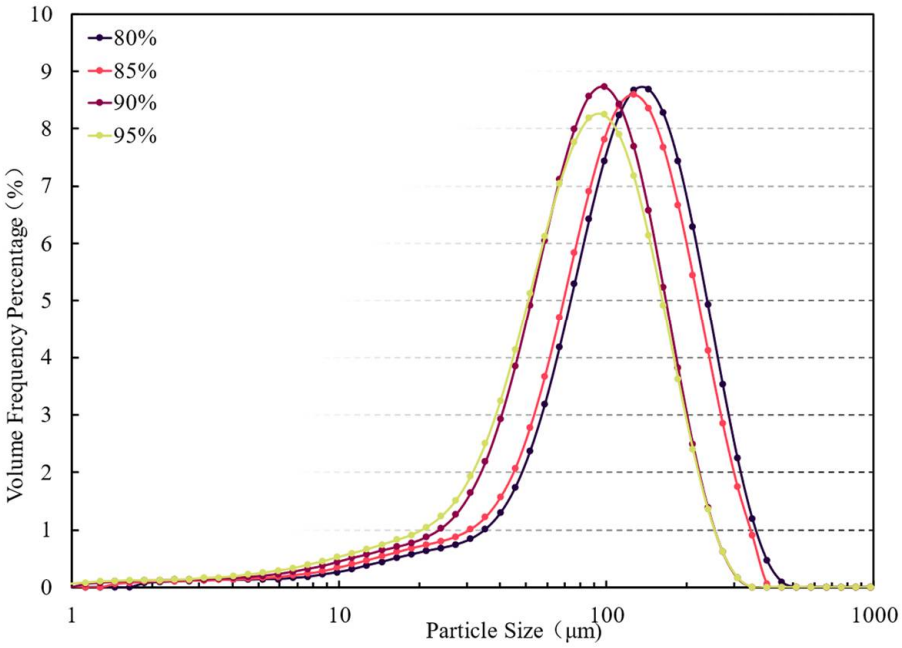


Figure 13. Particle-size frequency distributions at different upper cyclic stress limits.

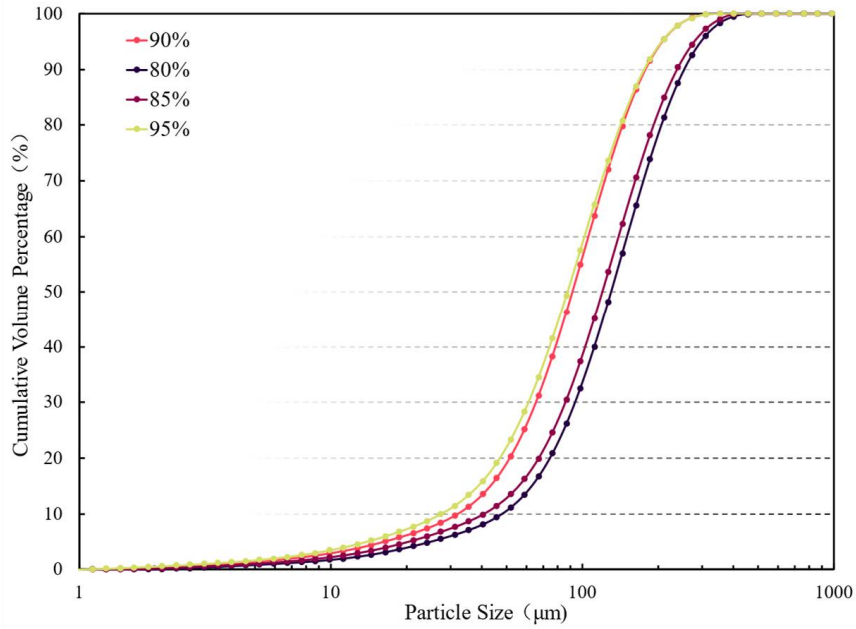


Figure 14. Particle-size cumulative distributions at different upper cyclic stress limits.

CT scanning was employed to compare borehole fracture features under different cyclic upper stress limits (Figure 15). As the upper stress limit increased, the V-shaped ("dog-ear") damage around the borehole expanded progressively. At an upper limit of 80%, the newly damaged area was 159.81 mm^2; this value increased slightly to 161.05 mm^2 at 85% and further to 173.61 mm^2 at 90%. A pronounced increase was observed at 95%, where the newly damaged area rose sharply to 264.26 mm^2, demonstrating a clear positive relationship between borehole damage area and the upper stress limit. Moreover, the radial fracture zones on both sides propagated deeper into the specimen with increasing stress level, indicating enhanced damage penetration and expansion of the damaged zone. The most substantial damage development, including the largest increment in the damaged area and the highest overall damage severity, occurred at the 95% upper stress limit.

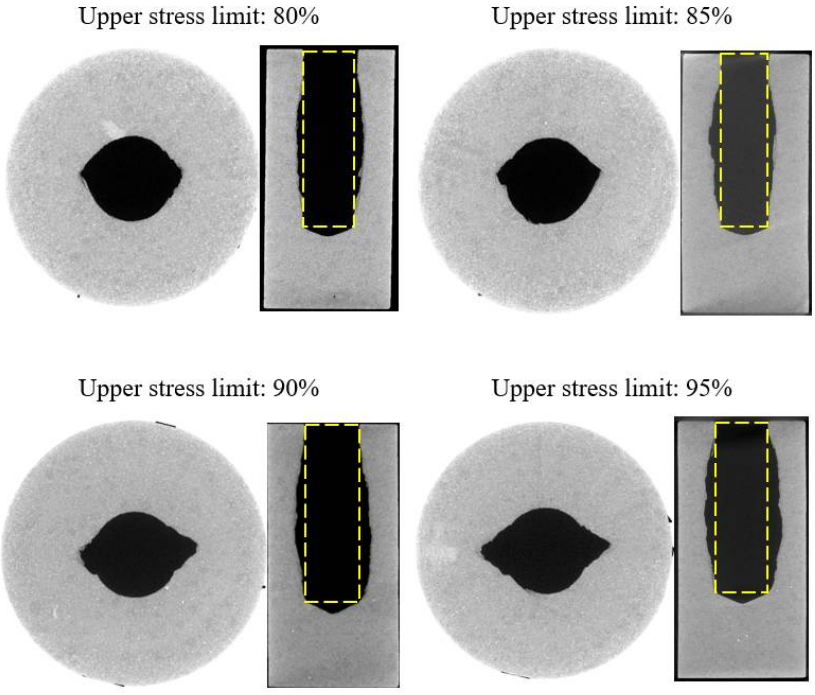


Figure 15. Hole damage at different upper cyclic stress limits.

3.3. Effects of Cycling Frequency on Sand Production

In addition to the loading stage and cyclic upper stress limit, cycling frequency can also influence sand production under cyclic loading. In this study, an injection–production frequency of 0.033 Hz was adopted as the reference condition, while three lower frequencies (0.017 Hz, 0.0033 Hz, and 0.001 Hz) were applied to quantify the frequency effect. Figure 16 presents the evolution of cumulative produced-sand mass at different frequencies. A clear trend is observed: the cumulative sand mass increases as the cycling frequency decreases. At 0.001 Hz, the cumulative sand mass is 53.1% higher than that under the reference condition. Figure 17 compares the particle-size fractions of the produced sand. Fine sand dominates at all tested frequencies, implying that cyclic loading preferentially mobilizes small particles from weakly cemented zones or intergranular boundary regions. With decreasing frequency (i.e., longer loading time per cycle), the fine-sand fraction increases initially and then decreases. Notably, at 0.0033 Hz and lower frequencies, the fine-sand fraction becomes relatively stable, with markedly reduced fluctuations. This behavior suggests that when the loading time scale is sufficiently long, the granular framework tends to evolve toward a new quasi-stable failure state, thereby reducing the sensitivity of particle-size partitioning to further frequency changes.

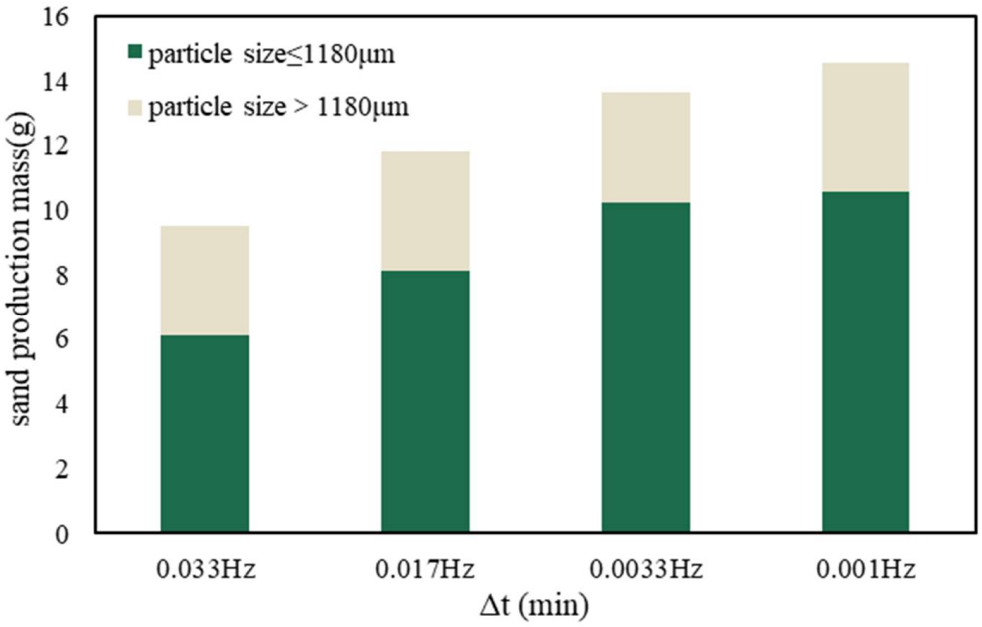


Figure 16. Cumulative sand production at different cycling frequencies.

Laser diffraction particle-size measurements were performed on the produced sand obtained under different cycling frequencies, and the particle-size frequency distribution and cumulative volume distribution curves are shown in Figure 18 to evaluate the effect of cyclic frequency on particle-size distribution. The particle-size frequency distributions exhibit a systematic shift toward finer sizes as the cycling frequency decreases, indicating that low-frequency cyclic loading facilitates particle breakage and the generation of finer fragments. Among the four cases, the 0.033 Hz group shows the rightmost peak, corresponding to comparatively coarser particles. In contrast, the 0.001 Hz group displays a pronounced shift in the peak toward smaller sizes, accompanied by generally higher volume fractions in the fine-size region, which suggests a stronger breakage intensity. The cumulative volume curves in Figure 19 further corroborate this trend: decreasing frequency results in a steeper rise in cumulative percentage, implying that a larger proportion of particles is concentrated in the fine-size range. Consistently, the median particle size (D50) decreases from 92.4 μm at 0.033 Hz to 89.9 μm at 0.017 Hz, 76.3 μm at 0.0033 Hz, and 72.5 μm at 0.001 Hz.

Overall, D50 decreases monotonically with decreasing cycling frequency, confirming that low-frequency cyclic loading more readily induces sand-particle breakage and produces finer particles. These observations demonstrate that cycling frequency exerts a clear control on the breakage characteristics of produced sand. This enhanced breakage under low-frequency loading is likely associated with longer loading–unloading durations per cycle, which provides more time for grain rearrangement, intergranular sliding/crushing, and progressive damage accumulation within the granular framework.

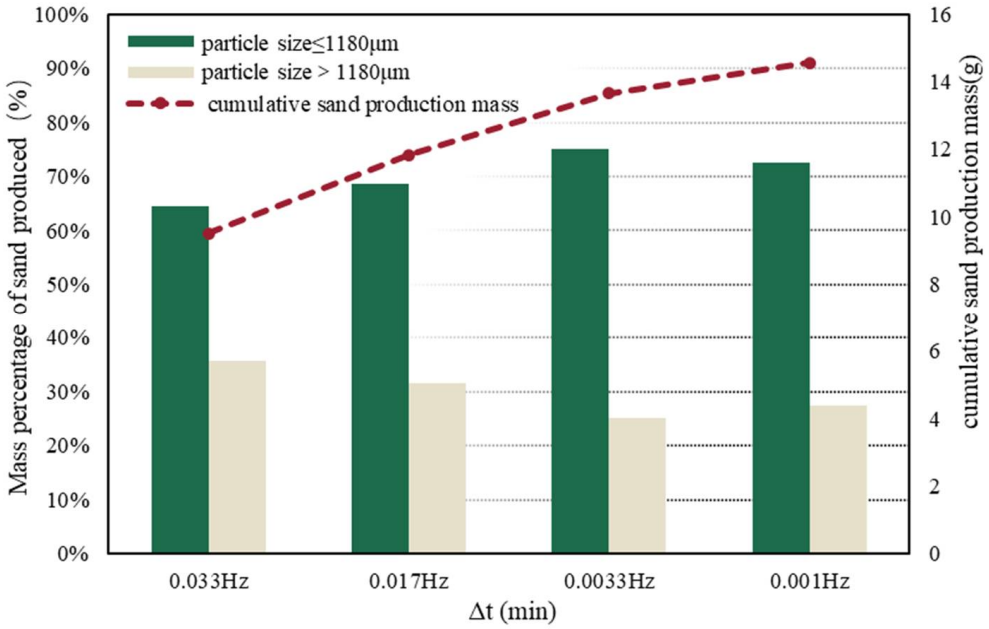


Figure 17. Mass fractions of produced sand in different particle-size ranges at different cycling frequencies.

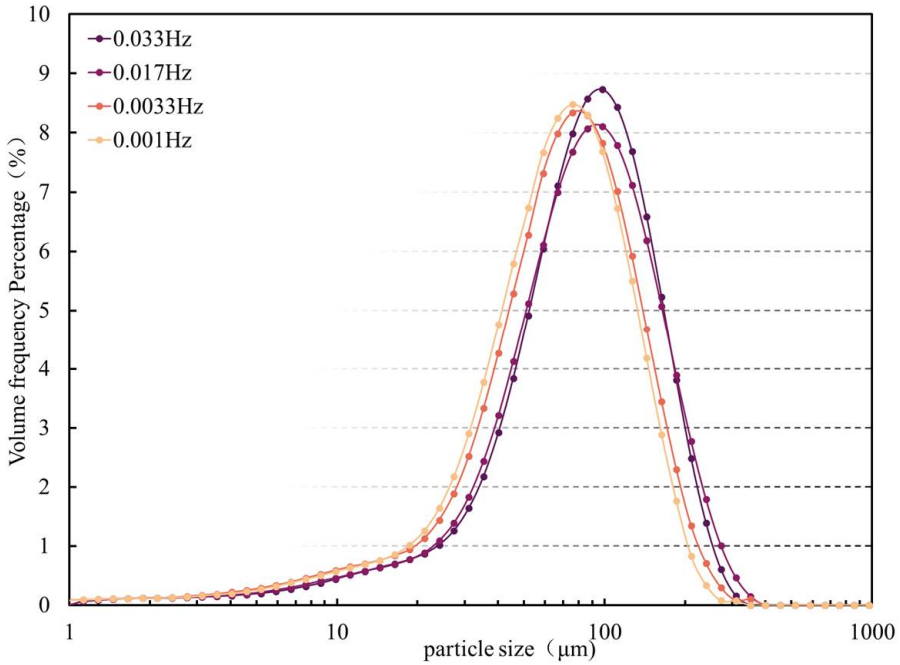


Figure 18. Particle-size frequency distributions at different cycling frequencies.

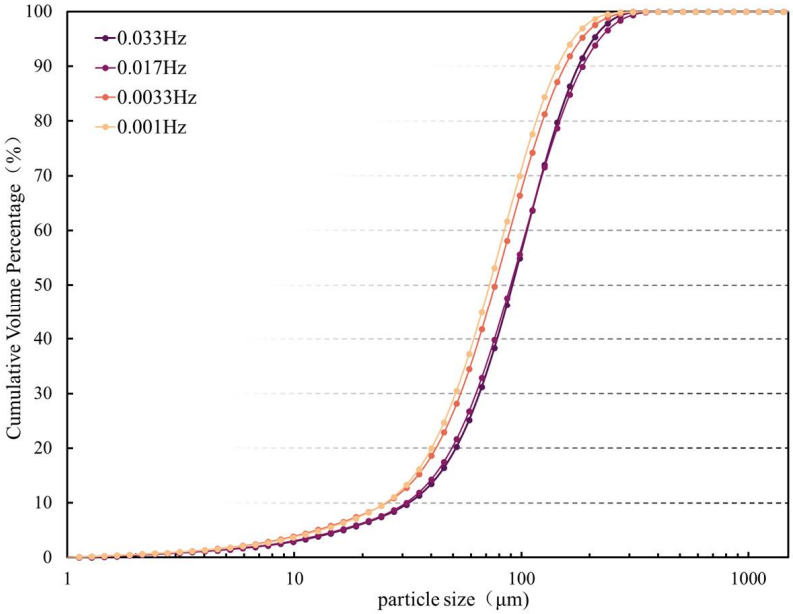


Figure 19. Particle-size cumulative distributions at different cycling frequencies.

CT imaging was used to characterize the evolution of borehole-related cracking under different cycling frequencies (Figure 20). Overall, cycling frequency exerts clear control on the extent of borehole damage, with a markedly larger crack-damaged zone developing under low-frequency loading. As the frequency decreases from 0.033 Hz to 0.001 Hz, the newly developed crack-damaged area around the borehole increases from 173.61 mm^2 to 293.49 mm^2, representing an increase of approximately 69%. This trend suggests that lower frequencies, which correspond to longer loading–unloading durations per cycle, provide more time for crack initiation and stable propagation, thereby enhancing cumulative damage.

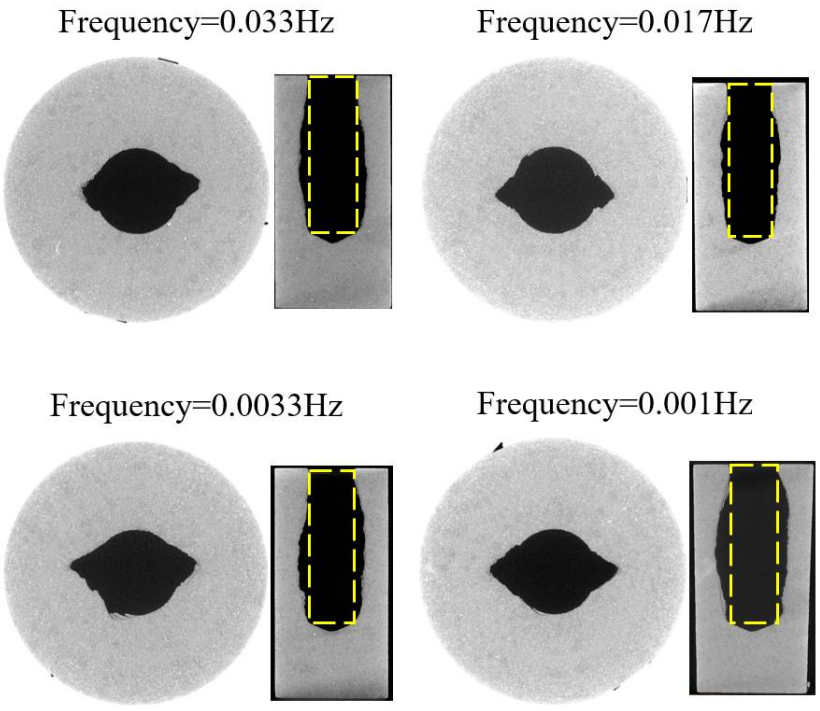


Figure 20. Hole damage at different cycling frequencies.

Regarding damage morphology, at higher frequencies (0.033 Hz and 0.017 Hz), cracking remains largely confined to the near-borehole region and exhibits a relatively compact V-shaped ("dog-ear") pattern. When the frequency decreases to 0.0033 Hz and 0.001 Hz, cracks propagate radially along both sides of the borehole, leading to pronounced expansion of the crack-damaged zone. In addition, the damage becomes more asymmetric and extends deeper into the specimen. These observations indicate that low-frequency cycling promotes more pronounced crack opening–closing and sustained stress concentration around the borehole, making local weak planes more susceptible to progressive failure under repeated tensile–shear loading. In summary, reducing cycling frequency increases the characteristic time scale of cyclic loading, which governs the rate of crack accumulation and the development path of the damage zone. Under low-frequency cycling, the longer time per cycle facilitates time-dependent deformation and progressive microstructural degradation, ultimately resulting in larger-scale borehole damage.

4. Conclusions

This study focuses on sand production induced by cyclic stress disturbances during injection–production cycling in underground gas storage (UGS). Laboratory sand-production tests under cyclic loading were conducted to systematically evaluate the effects of loading stage, upper stress limit, and cycling frequency on hole damage and sand-production behavior.

1. The cyclic-loading stage (rapid hardening, stable, failure, and collapse) strongly controls hole morphology and sand production. During the rapid-hardening and stable stages, the hole remains largely intact and sand production is negligible. Once the specimens enter the failure and collapse stages, hole integrity progressively degrades, and sand production increases sharply, with the collapse stage dominated by a rapid rise in fine sand. The coarse-sand mass changes only slightly, indicating that variations in total sand production are mainly governed by the fine-sand fraction. Consequently, stage-dependent sand control is recommended: early operations should focus on mitigating episodic coarse-particle release, whereas late-stage management should strengthen fine-sand handling. Concurrent monitoring of pressure-cycling behavior, sand mass, and particle-size distribution is suggested for early warning of accelerated deterioration.
2. Increasing the cyclic upper stress limit leads to a pronounced increase in cumulative sand production. When the upper limit rises from 80% to 95%, the cumulative produced sand mass increases by approximately 2.53 times. Meanwhile, the fine-sand fraction in the produced sand increases, and the overall particle-size distribution shifts toward smaller sizes. At an upper stress limit of 95%, the fine-sand fraction reaches 70.52%, indicating that increasing the cyclic upper stress limit not only increases the total produced-sand mass but also enhances particle-size refinement. Strict control of peak operating pressure, together with avoidance of rapid or excessive pressurization near the upper pressure limit, is essential for limiting cyclic damage accumulation and the associated risk of sand production.

The cycling frequency has a strong influence on both sand production and particle-size distribution. As the frequency decreases, the cumulative produced sand mass increases; at 0.001 Hz, sand production is 53.1% higher than that of the control. Lower-frequency cycling also increases the proportion of fine sand and results in more pronounced particle breakage. Consistently, the median particle size (D50) decreases with decreasing frequency, indicating that low-frequency cycling is more likely than high-frequency cycling to promote sand-particle fragmentation and generate finer particles. Accordingly, the injection–production

schedule and the pressurization/depressurization rates should be optimized, for example, by adopting smoother pressure ramps, to limit cyclic damage accumulation.

Author Contributions: For research conceptualization, W.Z. and S.T.; methodology, W.Z.; validation, H.Z., T.W., and J.X.; formal analysis, H.Z.; investigation, Y.T.; resources, S.T.; data curation, H.Z.; writing—original draft preparation, W.Z.; writing—review and editing, H.Z.; visualization, H.Z.; supervision, Y.T.; project administration, T.W.; funding acquisition, S.T. All authors have read and agreed to the published version of the manuscript.

Funding: The Innovative Research Group Project of the National Natural Science Foundation of China; No. 52421002.

Data Availability Statement: The data presented in this study are available on request from the corresponding author.

Conflicts of Interest: Author Junjie Xue was employed by Oil and Gas Technology Institute of Changqing Oilfield Company. The remaining authors declare that the research was conducted in the absence of any commercial or financial relationships that could be construed as a potential conflict of interest.

References

1. Zheng, D.; Wanyan, Q.; Zhao, K. Development Status and Prospect of Underground Natural Gas Storage in China. *Int. Pet. Econ.* **2025**, *33*, 37–45.
2. Ding, G.; Wang, J. Key Points in the Reconstruction of an Underground Gas Storage Based on a Depleted Gas Reservoir. *Nat. Gas Ind.* **2011**, *31*, 87–89.
3. Wanyan, Q.; Wang, Y.; Li, D.; Xu, H.; Li, C.; Li, K.; Li, J.; Li, L. Progress in Safety Construction and Operation Technologies for Underground Gas Storage under Complex Geological Conditions. *Oil Gas Storage Transp.* **2023**, *42*, 1092–1099.
4. Khalaf, M.S.; Rezaei, A.; Soliman, M.Y.; Farouq Ali, S.M. Thermo-Poroelastic Analysis of Cold Fluid Injection in Geothermal Reservoirs for Heat Extraction Sustainability. In Proceedings of the 56th U.S. Rock Mechanics/Geomechanics Symposium, Santa Fe, NM, USA, 26 June 2022.
5. Yuan, G.; Zhang, Y.; Dong, J.; Xia, Y.; Ban, F.; Guan, Y. New Development of Sand Production Theory and Technology in Oil and Gas Wellbores. *Sci. Technol. Eng.* **2023**, *23*, 2694–2704.
6. Tian, S.; Zhang, W.; Weng, J.; Guan, Z.; Wang, J.; Liu, D. Mechanism of Sand Production under Alternating Injection–Production Mode during the Conversion of Xinjiang MH Gas Reservoir to Underground Gas Storage. *Xinjiang Oil Gas* **2024**, *20*, 56–62.
7. Ma, X.; Zheng, D.; Shen, R.; Wang, C.; Luo, J.; Sun, J. Key Technologies and Practice for Gas Field Storage Facility Construction under Complex Geological Conditions in China. *Pet. Explor. Dev.* **2018**, *45*, 489–499. [CrossRef]
8. Qin, Y.; Xie, R.; Feng, D.; Mi, J.; Lu, H.; Liu, J. Research Progress on Mechanism and Control Method of Sand Production of Underground Gas Storage in Depleted Reservoir. *Petrochem. Ind. Appl.* **2024**, *43*, 1–7.
9. Liao, W.; Luo, S.; Hu, S.; Zhang, Y.; Luo, H. A New Method for the Study of Sand Production in Gas Reservoir Storage. *J. Southwest Pet. Univ. Sci. Technol. Ed.* **2023**, *45*, 119–130.
10. Slagle, D.M.; Ward, R.W.; Reed, L.N.; Wallen, D.A.; Ledet, C.A. Control of Sand Production in the Underground Storage of Natural Gas. *J. Pet. Technol.* **1969**, *21*, 581–586. [CrossRef]
11. Naderloo, M.; Ramesh Kumar, K.; Hernandez, E.; Hajibeygi, H.; Barnhoorn, A. Experimental and Numerical Investigation of Sandstone Deformation under Cycling Loading Relevant for Underground Energy Storage. *J. Energy Storage* **2023**, *64*, 107198. [CrossRef]
12. Kang, Y.; Shao, J.; You, L.; Gao, X.; Chen, M.; Tan, Q.; Han, H. Experimental Simulation on Fine Migration Induced by the Violent Change of Gas Injection Pressure of Gas Storage Well. *Oil Drill. Prod. Technol.* **2020**, *42*, 797–803. [CrossRef]
13. Dong, C.; Chen, C.; Zhou, B.; Sui, Y.; Wang, X.; Wang, J. Sand Production Mechanism and Sand Control Technology Status and Prospect of Oil and Gas Reservoir Type Gas Storage. *Oil Drill. Prod. Technol.* **2022**, *44*, 43–55. [CrossRef]
14. Sui, Y.; Lin, T.; Liu, X.; Zhao, Z.; Liu, J.; Wang, Y. Effect of Alternating Load on Sand Production of Injection–Production Wells in Gas Storage. *Oil Gas Storage Transp.* **2019**, *38*, 303–307. [CrossRef]
15. Ma, L.; Dong, J.; Wang, J.; Zhang, Y.; Li, G.; Li, J. Sand Production Prediction of Depleted-Reservoir Underground Gas Storage—An Experimental Study. In *Proceedings of the 56th U.S. Rock Mechanics/Geomechanics Symposium, Santa Fe, NM, USA, 26 June 2022*; ARMA: Santa Fe, NM, USA, 2022; Paper Number: ARMA-2022-0103.
16. McLellan, P.J.; Hawkes, C.D.; Read, R.S. Sand Production Prediction for Horizontal Wells in Gas Storage Reservoirs. In Proceedings of the SPE/CIM International Conference on Horizontal Well Technology, Calgary, AL, Canada, 6–8 November 2000.

17. Zhang, Y.; Yuan, G.; Dong, J.; Liu, T.; Qiu, Y.; Wu, Q.; Zang, C.; Ding, J. Experimental Study on Sand Production of Depleted Oil and Gas Reservoirs. *Front. Earth Sci.* **2023**, *11*, 1136695. [CrossRef]
18. Liao, W. Experimental Simulation on the Influencing Factors of Sand Production in H Gas Storage, Xinjiang, China. *ACS Omega* **2021**, *6*, 31727–31737. [CrossRef] [PubMed]
19. Hou, Q.; Wei, J.; Qiu, P.; Zhou, X.; Gayubov, A. Experimental Study on Sand Production Mechanism of Underground Gas Storage in Depleted Reservoir. *J. Phys. Conf. Ser.* **2023**, *2610*, 012024. [CrossRef]
20. Song, R.; Xie, R.; Zhang, P.; Pei, G.; Liu, J.; Wan, X. Critical Drawdown Pressure Prediction for Sanding Production of Underground Gas Storage in a Depleted Reservoir in China. *Energy Sci. Eng.* **2023**, *11*, 4287–4301. [CrossRef]
21. Tian, D. Research on Sand Production Characteristics of Gas Storage in Depleted Oil and Gas Reservoirs. Master's Thesis, China University of Petroleum (Beijing), Beijing, China, 2021.
22. Johari, A.K.; Busahmin, B.; Tyson, S. Prediction of Spatial Variability in Grain Size Distribution on Outcrop from Gamma Ray Measurement. *Pet. Coal* **2024**, *66*, 914–922.
23. Matarsa, R.A.; Busahmin, B. Permeability Measurements Facilitate the Assessment of Spatial Differences in Grain Size Distributions Present in an Outcrop. *Pet. Coal* **2025**, *67*, 207–214.
24. Hatheway, A.W. The Complete ISRM Suggested Methods for Rock Characterization, Testing and Monitoring: 1974–2006. *Environ. Eng. Geosci.* **2009**, *15*, 47–48. [CrossRef]
25. Papamichos, E. Sand Mass Prediction in a North Sea Reservoir. In Proceedings of the SPE/ISRM Rock Mechanics Conference, Irving, TX, USA, 20–23 October 2002. [CrossRef]
26. He, Y.; Ma, H.; Tan, X.; Chen, L.; Wan, J.; Yue, R.; Yi, X. Mechanical Properties and Sealing Performance Evaluation of Packers in High Temperature Underground Gas Storage. *Sci. Rep.* **2025**, *15*, 20925. [CrossRef] [PubMed]
27. Wanyan, Q.; Xu, H.; Song, L.; Zhu, W.; Pei, G.; Fan, J.; Zhao, K.; Liu, J.; Gao, Y. A Novel Performance Evaluation Method for Gas Reservoir-Type Underground Natural Gas Storage. *Energies* **2023**, *16*, 2640. [CrossRef]
28. Yan, M.; Deng, J.; Yu, B.; Li, M.; Zhang, B.; Xiao, Q.; Tian, D. Comparative Study on Sanding Characteristics between Weakly Consolidated Sandstones and Unconsolidated Sandstones. *J. Nat. Gas Sci. Eng.* **2020**, *76*, 103183. [CrossRef]

Disclaimer/Publisher's Note: The statements, opinions and data contained in all publications are solely those of the individual author(s) and contributor(s) and not of MDPI and/or the editor(s). MDPI and/or the editor(s) disclaim responsibility for any injury to people or property resulting from any ideas, methods, instructions or products referred to in the content.